Resolving the discrepancy between X-ray and gravitational lensing mass measurements for clusters of galaxies

S. W. Allen

Institute of Astronomy, Madingley Road, Cambridge CB3 0HA

ABSTRACT

We present a detailed comparison of mass measurements for clusters of galaxies using *ASCA* and *ROSAT* X-ray data and constraints from strong and weak gravitational lensing. Our results, for a sample of 13 clusters (including six with massive cooling flows, five without cooling flows, and two intermediate systems), provide a consistent description of the distribution of gravitating matter in these systems. For the six cooling-flow clusters, which are the more dynamically relaxed systems, the X-ray and strong gravitational lensing mass measurements show excellent agreement. The core radii for the mass distributions are small, with a mean value (using a simple isothermal parametrization) of $\sim 50 h_{50}^{-1}$ kpc. These results imply that thermal pressure dominates over non-thermal processes in the support of the X-ray gas against gravity in the central regions of the cooling-flow clusters, and that the hydrostatic assumption used in the X-ray mass determinations is valid.

For the non-cooling-flow clusters, the masses determined from the strong-lensing data exceed the X-ray values by factors of $2-4$. However, significant offsets between the X-ray and lensing centres are observed, indicating that the X-ray and strong-lensing data are probing different lines of sight through the clusters. These offsets, and the generally complex dynamical states of the clusters inferred from their X-ray morphologies, lensing data and galaxy distributions, suggest that the gravitational potentials in the central regions of the non-cooling-flow systems are evolving rapidly, and that the assumption of hydrostatic equilibrium involved in the X-ray mass measurements is likely to have broken down. The discrepancies between the X-ray and strong-lensing mass measurements may be reconciled if the dynamical activity has caused the X-ray analyses to overestimate the core radii of the dominant mass clumps in the clusters. Substructure and line-of-sight alignments of material towards the cluster cores may also contribute to the discrepancies since they will increase the probability of detecting gravitational arcs in the clusters and can enhance the lensing masses, without significantly affecting the X-ray data. On larger spatial scales, comparisons of the X-ray mass results with measurements from weak gravitational lensing show excellent agreement for both cooling-flow and non-cooling-flow clusters.

Our method of analysis accounts for the effects of cooling flows on the X-ray data. We highlight the importance of this and show how the inappropriate use of simple isothermal models in the analysis of X-ray data for clusters with massive cooling flows will result in significant underestimates of the virial temperatures and masses of these systems.

Key words: galaxies: clusters: general – cooling flows – intergalactic medium – gravitational lensing – X-rays: galaxies.

1 INTRODUCTION

Accurate measurements of the masses of clusters of galaxies provide a crucial observational constraint on cosmological models. Clusters are the largest gravitationally-bound objects known and represent rare peaks in the primordial density field on spatial scales of order 10 Mpc. The number densities and spatial distributions of clusters in a given mass range can be directly related to cosmological simulations and semi-analytic models (e.g. Frenk et al. 1990; Evrard 1990; Henry & Arnaud 1991; White, Efstathiou & Frenk 1993; Viana & Liddle 1996; Eke, Cole & Frenk 1996; Kitayama & Suto 1996; Oukbir & Blanchard 1997; Oukbir, Bartlett

& Blanchard 1997). Historically, measurements of the masses of clusters were made from optical studies of their galaxy populations. However, such studies are complicated by the presence of complex galaxy orbits, substructure (resulting from the growth of clusters through merger events) and projection effects (Lucey 1983; Sutherland 1988; Frenk et al. 1990; van Haarlem, Frenk & White 1997).

Currently, the two most promising techniques for obtaining accurate measurements of cluster masses are via X-ray observations and observations of gravitational lensing by clusters. Clusters of galaxies are luminous X-ray sources, with typical luminosities ranging from a few $\times 10^{43} - 10^{46}$ erg s^{-1}. The X-rays from clusters are primarily bremsstrahlung emission from the diffuse intracluster medium (ICM) that fills the deep gravitational potentials. The mass in X-ray gas exceeds the visible stellar mass by a factor of $1 - 5$, and typically contributes between 10 and 30 per cent of the total mass of the cluster (with the largest values observed for the most massive systems: David, Jones & Forman 1995; White & Fabian 1995). The X-ray emissivity is proportional to the square of the gas density and accurately traces the three-dimensional cluster potentials. X-ray observations thus offer a method for identifying clusters and determining cluster masses that is comparatively free from the projection effects that complicate the optical studies (Gioia et al. 1990; Ebeling et al. 1996, 1997).

Measurements of the masses of clusters from the X-ray data are based on the assumption that the ICM is in hydrostatic equilibrium with the gravitational potential of the cluster. The total mass profile is determined once the radial profiles of the gas density and temperature are known. The gas density profile can be accurately determined from X-ray images. Measurements of the temperature profile, however, require detailed spatially resolved spectroscopy. Although radial temperature profiles have been determined for a few clusters (e.g. Allen & Fabian 1994; Nulsen & Böhringer 1995; Markevitch & Vikhlinin 1997), in general the constraints are not firm and significant uncertainties remain, particularly in the outer ($r > 1$ Mpc) regions of clusters. For most systems only a mean emission-weighted X-ray temperature, determined from an integrated cluster spectrum, is available. More precise information on the temperature profiles of clusters will become available in the near future, following the launch of *AXAF*.

In contrast to the aforementioned optical galaxy dispersion and X-ray techniques, gravitational lensing offers a method for measuring the projected surface density of matter through clusters that is essentially free from assumptions about the dynamical state of the gravitating material (Fort & Mellier 1994). Recently, a number of studies have compared mass measurements for clusters, using the X-ray and gravitational lensing techniques. Miralda-Escudé & Babul (1995) presented an analysis of the clusters Abell 1689 and Abell 2218 and noted a discrepancy of a factor $\sim$2 between the X-ray and strong-lensing mass determinations for these systems. Miralda-Escudé & Babul (1995) suggested a number of possible explanations for the observed discrepancy: (i) the clusters could have prolate ellipsoidal mass distributions; (ii) a superposition of mass clumps along the lines of sight through the systems; (iii) the X-ray gas could have a complex, non-isothermal temperature structure; (iv) bulk and/or turbulent motions or magnetic fields could contribute significantly to the support of the ICM against gravity [this point was also explored by Loeb & Mao (1994) who suggested that non-thermal pressure support could completely account for the X-ray/strong-lensing mass discrepancy in Abell 2218]; (v) the multiphase nature of the central ICM could result in significant differences between emission-weighted and mass-weighted temperatures for clusters, potentially biasing X-ray

mass measurements to low values. The importance of this final point was discussed in detail by Waxman & Miralda-Escudé (1995), and will be further addressed in this paper.

Wu & Fang (1997) compared mass estimates from optical galaxy dispersions, gravitational lensing and X-ray methods for a large sample of data drawn from the literature. These authors concluded that the mass measurements from the galaxy dispersions and lensing data were generally in agreement, but were typically a factor of $2-3$ larger than the X-ray-determined values. These authors suggested that non-thermal pressure support in the ICM, or simplifying assumptions employed in their X-ray analysis, were likely to be responsible for the observed discrepancy.

Bartelmann & Steinmetz (1996) used gas-dynamical simulations to investigate the biases impinging on detections of strong gravitational lensing by clusters of galaxies. These authors showed that clusters selected for their strong-lensing properties are typically more dynamically active than average clusters, with arcs occurring preferentially in clusters exhibiting substructure and non-equilibrium states. Bartelmann & Steinmetz (1996) concluded that in those clusters in which the X-ray-determined mass is not equal to the strong-lensing mass, the discrepancy is primarily due to enhancements of the lensing mass via projection effects.

Comparisons of weak lensing and X-ray mass measurements for clusters provide a somewhat contrasting view to that obtained with the strong-lensing data. Although few detailed comparisons have been made to date, in general such studies have inferred good agreement between the weak-lensing and X-ray determined masses, e.g. the studies of Abell 2218 and Abell 2163 by Squires et al. (1996, 1997a). Smail et al. (1997) present weak-lensing masses for twelve $z \sim 0.4$ clusters imaged with the *Hubble Space Telescope* (*HST*) and demonstrate reasonable agreement with the masses estimated from their X-ray luminosities and the empirical L_X/T_X relation.

X-ray observations of clusters of galaxies show that in the central regions of most (70−90 per cent) clusters, the cooling time of the ICM is significantly less than the Hubble time (Edge, Stewart & Fabian 1992; White, Jones & Forman 1997; Peres et al. 1997). The observed cooling leads to a slow net inflow of material towards the cluster centre, a process known as a cooling flow (Fabian 1994). The X-ray imaging data show that gas typically 'cools out' throughout the central few tens to hundreds of kpc in the clusters, with $\dot{M}(r) \propto r$, where $\dot{M}(r)$ is the integrated mass deposition rate within radius r. Recent spatially resolved X-ray spectroscopy has confirmed the presence of distributed cool (and rapidly cooling) gas in cooling flows, with a spatial distribution and luminosity in excellent agreement with the predictions from the imaging data (Allen & Fabian 1997). The natural state for a regular, relaxed cluster of galaxies appears to be with a cooling flow in its core. Once established, only a major merger event is likely to disrupt the central regions of a cluster to the extent that a cooling flow is 'turned-off' (McGlynn & Fabian 1984; Edge et al. 1992).

In their combined X-ray and strong gravitational lensing study of the massive cooling-flow cluster PKS0745−191, Allen, Fabian & Kneib (1996a) demonstrated the importance of accounting for the effects of cooling flows on determinations of cluster masses from the X-ray data. These authors demonstrated excellent agreement between X-ray and strong-lensing masses for PKS0745−191, once the multiphase nature of the X-ray emission from the cooling flow was accounted for. In contrast, when more simple single-phase analyses of the X-ray data are employed (as has been the case in most previous studies) the total mass within the critical lensing radius can be underestimated by as much as a factor $\sim$3. This point

was further illustrated in the study of the more distant, massive cooling-flow cluster Abell 1835 by Allen et al. (1996b). Both PKS0745–191 and Abell 1835 appear dynamically relaxed at optical and X-ray wavelengths, in comparison to many other famous lensing systems such as Abell 1689 and Abell 2218.

In this paper we present a detailed comparison of X-ray and lensing mass measurements for 13 clusters of galaxies. Our sample includes six strong cooling flows, five non-cooling flows and two intermediate systems (where the classifications are made according to the fraction of the X-ray luminosity from the clusters contributed by their cooling flows). We explore the relationships between the dynamical states of the clusters (which relate to the presence or absence of cooling flows in these systems, as well as their morphological properties; Buote & Tsai 1996b) and X-ray and gravitational-lensing measurements of their masses. We show how taking full account of the various processes affecting the X-ray measurements can lead to a consistent picture for the distribution of gravitating matter in these systems. Throughout this paper, we assume $H_0 = 50 \, \mathrm{km\,s^{-1}\,Mpc^{-1}}$, $\Omega = 1$ and $\Lambda = 0$.

2 OBSERVATIONS AND DATA REDUCTION

Our sample consists of those clusters reported in the literature to exhibit strong gravitational lensing, for which (at the time of writing) high-quality *ASCA* X-ray spectra and *ROSAT* High Resolution Imager (HRI) images, were available on the Goddard Space Flight Centre (GSFC) public archive (with the exception of the HRI image of RXJ1347.5-1145, which was kindly provided by H. Böhringer & S. Schindler).

The *ASCA* (Tanaka, Inoue & Holt 1994) observations were made over a two-and-a-half year period between 1993 April and 1995 November. The *ASCA* X-ray Telescope array (XRT) consists of four nested-foil telescopes, each focused on to one of four detectors; two X-ray CCD cameras, the solid-state imaging spectrometers (SIS: S0 and S1), and two gas scintillation imaging spectrometers (GIS: G2 and G3). The XRT provides a spatial resolution of ~3 arcmin half power diameter (HPD) in the energy range 0.3 − 12 keV. The SIS detectors provide excellent spectral resolution [$\Delta E/E = 0.02(E/5.9\,\mathrm{keV})^{-0.5}$] over a 22×22 arcmin^2 field of view. The GIS detectors provide poorer energy resolution [$\Delta E/E = 0.08(E/5.9\,\mathrm{keV})^{-0.5}$] over a larger circular field of view of ~50 arcmin diameter. Screened event lists were extracted from the *ASCA* archive and were reduced using the FTOOLS package developed and supported by GSFC. Standard reduction procedures, as recommended in the GSFC *ASCA* Data Reduction Guide, were followed, including appropriate grade selection, gain corrections and (where necessary) manual screening based on the individual instrument light curves.

The *ROSAT* HRI observations were carried out between 1991 November and 1995 June. The HRI provides a ~5 arcsec (full width at half-maximum) X-ray imaging facility (David et al. 1996). Reduction of the data was carried out with the Starlink ASTERIX package. X-ray images were extracted on a 2×2 arcsec^2 pixel scale, from which centres for the cluster X-ray emission were determined. Where more than one observation of a source was made, a mosaicked image was constructed from the individual observations. For the cooling-flow and intermediate clusters, the X-ray centres were identified with the peaks of the X-ray surface brightness distributions, which are easily determined from the HRI images. For the non-cooling flow clusters the X-ray emission is not as sharply-peaked, and for these systems we identify the X-ray centres with the results from iterative determinations of the centroids of the

emission within a 2 arcmin radius of the cluster centres. (For Abell 2163 and AC114, a 1-arcmin radius aperture was better suited and was used. For Abell 2744, 2218 and 2219 the use of either a 1 or 2 arcmin aperture does not significantly affect the determinations of the X-ray centres).

We note here that the lensing cluster Abell 370 also has *ASCA* and *ROSAT* HRI data available on the GSFC public archive but was not included in our sample because the HRI data show that it is not a single, coherent structure but rather consists of a number of individual subclumps. The assumptions of spherical symmetry and hydrostatic equilibrium required for the X-ray mass modelling will therefore not apply. The X-ray images for the other clusters included in the present sample do not exhibit any dramatic substructure that would clearly invalidate such assumptions. We note, however, the presence of an X-ray luminous subcluster, approximately 2.6 arcmin (850 kpc) to the northwest of Abell 2744 (AC118), visible in the HRI data. This subcluster is also identified in the weak lensing analysis of Smail et al. (1997).

The details of the *ASCA* and *ROSAT* observations are summarized in Tables 1 and 2, respectively. The basic X-ray properties of the target clusters are summarized in Table 3.

3 ANALYSIS

The lensing clusters studied in this paper are drawn from a larger sample of X-ray luminous systems discussed by Allen et al. (in preparation). A more detailed description of the X-ray analysis is included in that work, and only a brief summary is presented here. The method of X-ray analysis follows the multiphase technique employed in the studies of PKS0745–191 and Abell 1835 by Allen et al. (1996a,b). A re-analysis of both of these clusters is included in the current work.

For the purposes of this paper, clusters are classified into three categories; cooling flows, non-cooling flows and intermediate systems. The cooling flows are those clusters with central cooling times $< 5 \times 10^9$ yr and for which the flux from cooling gas is spectrally determined to account for $\gtrsim 20$ per cent of the total X-ray luminosity. Intermediate clusters are those systems with central cooling times $< 10^{10}$ yr and for which the cooling flows are spectrally determined to contribute < 20 per cent of the total X-ray luminosity. Non-cooling flow systems are those clusters

Table 1. *ASCA* observations.

Cluster	Date	S0	S1	G2	G3
Abell 2744	1994 Jul 04	37605	26086	62749	62753
PKS0745-191	1993 Nov 06	29146	——	37553	37553
Abell 963	1993 Apr 22	29611	29039	29883	29881
Abell 1689	1993 Jun 26	29575	23642	37817	37817
RXJ1347.5-1145	1995 Jan 17	27882	17549	38968	38958
MS1358.4+6245	1995 Apr 27	32532	30815	31981	31513
Abell 1835	1994 Jul 20	34927	33976	33876	33870
Abell 2163	1993 Aug 08	25126	18224	32760	32322
Abell 2218	1993 Apr 30	28241	26054	37970	37968
Abell 2219	1994 Aug 07	32705	31697	35849	35849
MS2137.3-2353	1994 May 08	15167	15732	17035	17056
Abell 2390	1994 Nov 13	6172	2632	10340	10338
AC114	1995 Nov 09	36739	36295	35987	35971

Notes: A summary of the *ASCA* observations. Column 2 lists the date of observation. Columns 3−6 list the effective exposure times (in seconds) for the four *ASCA* detectors.

Table 2. *ROSAT* HRI observations.

Cluster	Date	HRI	R.A. (J2000.)	Dec. (J2000.)
Abell 2744	1994 Dec 09	34256	$00^h14^m18.7^s$	$-30°23'11''$
PKS0745-191	1992 Oct 20	23750	$07^h47^m31.1^s$	$-19°17'47''$
Abell 963	1992 Nov 24	10104	$10^h17^m03.4^s$	$39°02'51''$
Abell 1689	1994 Jul 22/1995 Jun 24	22728	$13^h11^m29.1^s$	$-01°20'40''$
RXJ1347.5-1145	1995 Jan 28	15760	$13^h47^m31.0^s$	$-11°45'11''$
MS1358.4+6245	1993 May 14	15872	$13^h59^m50.8^s$	$62°31'05''$
Abell 1835	1993 Jan 22	2850	$14^h01^m02.0^s$	$02°52'40''$
Abell 2163	1994 Aug 13	36248	$16^h15^m45.9^s$	$-06°08'58''$
Abell 2218	1994 Jan 05 – 1994 Jun 17	92856	$16^h35^m52.5^s$	$66°12'29''$
Abell 2219	1994 Jan 17	13242	$16^h40^m20.2^s$	$46°42'29''$
MS2137.3-2353	1994 Apr 24	13656	$21^h40^m15.2^s$	$-23°39'41''$
Abell 2390	1993 Nov 23	27764	$21^h53^m36.5^s$	$17°41'45''$
AC114	1993 May 17/1994 May 09	23192	$22^h58^m48.7^s$	$-34°48'19''$

Notes: A summary of the *ROSAT* HRI observations. Columns 2 and 3 list the date of observation and exposure time (in seconds). Columns 4 and 5 list the coordinates of the centres of the X-ray emission from the clusters.

3.1 X-ray spectral analysis

Spectra were extracted from all four *ASCA* detectors (except for PKS0745-191, for which the S1 data were lost due to chip saturation problems) in circular regions, centred on the X-ray centroids (Table 2). For the SIS data, the radii of the regions were adjusted to minimize the number of chip boundaries crossed (thereby minimizing the systematic uncertainties introduced by such crossings) whilst covering as large a region of the clusters as possible. Data from the regions between the chips were masked out and excluded. For the GIS data a constant extraction radius of 6 arcmin was used.

For the GIS observations, and SIS observations of clusters in regions of low Galactic column density ($N_H < 5 \times 10^{20}$ atom cm^{-2}), background subtraction was carried out using the 'blank sky' observations of high Galactic latitude fields compiled during the performance verification stage of the *ASCA* mission. For such data sets, the blank sky observations provide a reasonable representation

with central cooling times $> 10^{10}$ yr, and which show no spectral evidence for cooling-flow emission. For full details see Allen et al. (in preparation).

Table 3. X-ray properties of the cluster sample.

	z	N_H (10^{20} atom cm^{-2})	$L_{X,2-10}$ (10^{44} erg s^{-1})	kT (keV)	$\dot{M}_{Spec}$ ($M_\odot$ yr^{-1})	ΔN_H (10^{20} atom cm^{-2})
COOLING FLOWS						
PKS0745-191	0.103	42.4	29.5	$8.7^{+1.6}_{-1.2}$	1460^{+350}_{-520}	28^{+11}_{-13}
RXJ1347.5-1145	0.451	4.9	93.5	$26.4^{+7.8}_{-12.3}$	3480^{+340}_{-1150}	27^{+30}_{-7}
MS1358.4+6245	0.327	1.9	10.5	$7.5^{+7.1}_{-1.5}$	690^{+350}_{-290}	64^{+87}_{-38}
Abell 1835	0.252	2.3	44.9	$9.8^{+2.3}_{-1.3}$	1760^{+520}_{-590}	32^{+16}_{-8}
MS2137.3-2353	0.313	3.6	16.6	$5.2^{+1.8}_{-0.7}$	1470^{+880}_{-730}	62^{+61}_{-28}
Abell 2390	0.233	6.8	41.0	$14.5^{+15.5}_{-5.2}$	1530^{+580}_{-1110}	29^{+76}_{-15}
INTERMEDIATE						
Abell 963	0.206	1.4	12.7	$6.13^{+0.45}_{-0.30}$	—	—
Abell 1689	0.184	1.8	32.2	$10.0^{+1.2}_{-0.8}$	350^{+290}_{-210}	41^{+56}_{-18}
NON COOLING FLOWS						
Abell 2744	0.308	1.6	30.9	$7.75^{+0.59}_{-0.53}$	—	—
Abell 2163	0.208	12.1	60.1	$10.85^{+0.71}_{-0.63}$	—	—
Abell 2218	0.175	3.2	10.8	$7.18^{+0.50}_{-0.45}$	—	—
Abell 2219	0.228	1.8	38.0	$9.46^{+0.63}_{-0.57}$	—	—
AC114	0.312	1.3	17.2	$8.10^{+1.01}_{-0.85}$	—	—

Notes: Columns 2 and 3 list the cluster redshifts and Galactic column densities (from Dickey & Lockman 1990). $L_{X,2-10}$ values are the X-ray luminosities in the $2 - 10$ keV restframe of the source, determined from the G3 spectra. For the cooling-flow and intermediate clusters, the temperatures (kT) were determined with a spectral model incorporating an intrinsically-absorbed, cooling-flow component. For the non-cooling systems, a more simple isothermal model with free-fitting absorption (assumed to lie at zero redshift) was used. Column 6 lists the mass deposition rates from the cooling flows determined from the *ASCA* spectra and column 7 the intrinsic absorbing column densities determined to act on the cooling flows. Errors bars are 90 per cent ($\Delta\chi^2 = 2.71$) confidence limits on a single interesting parameter. Where no value for the mass deposition rate is listed, this component was not statistically required by the data.

of the cosmic and instrumental backgrounds in the detectors. The background data were screened and grade selected in the same manner as the target observations and background spectra were extracted over the same regions as the cluster spectra. For the SIS observations of clusters in directions of higher Galactic column density (PKS0745−191, Abell 2163, Abell 2390), background spectra were extracted from regions of the chips that were relatively free from foreground cluster emission.

For the SIS data, response matrices were generated using the FTOOLS SISRMG software. Where the spectra covered more than one chip, response matrices were created for each chip; these matrices were then combined to form a counts-weighted mean matrix. For the GIS analysis, the response matrices issued by GSFC on 1995 March 6 were used.

Modelling of the X-ray spectra was carried out using the XSPEC spectral fitting package (version 9.0; Arnaud 1996). For the SIS data, only counts in pulse height analyser (PHA) channels corresponding to energies between 0.6 and 10.0 keV were included in the analysis (the energy range over which the calibration of the SIS instruments is best understood). For the GIS data, only counts in the energy range $1.0 - 10.0$ keV were used. The spectra were grouped before fitting to ensure a minimum of 20 counts per PHA channel, allowing χ^2 statistics to be used.

The spectra have been modelled using the plasma codes of Kaastra & Mewe (1993; incorporating the Fe L calculations by Liedhal in XSPEC version 9.0) and the photoelectric absorption models of Balucinska-Church & McCammon (1992). The spectra were examined with a series of models. For clarity, in this paper we only report those relevant results from the best-fitting models. (A more complete discussion is given by Allen et al., in preparation). The data from all four *ASCA* detectors were fitted simultaneously, with the parameters forced to take the same values across the data sets. The exceptions to this were the emission measures of the cluster gas in the different detectors which, due to the different extraction radii used (and residual uncertainties in the flux calibration of the instruments), were included as independent fit parameters.

The non-cooling flow clusters were found to be well-described by a simple isothermal plasma model, where the temperature, metallicity, absorbing column density and emission measures were included as free parameters in the fits. The best-fitting column densities for the non-cooling flow clusters were generally found to be in reasonable agreement with the Galactic values, although the former were, typically, slightly higher (Allen et al., in preparation; see also Section 4.2). In contrast, the cooling-flow clusters required the introduction of a second emission component with a lower mean temperature, which was also required to be intrinsically absorbed. For consistency with the imaging analysis presented in Section 3.2 we have modelled this cooler component as a constant pressure cooling flow, in which gas is assumed to cool from the ambient cluster temperature, following the prescription of Johnstone et al. (1992). (This is model is referred to as spectral model C by Allen et al., in preparation). The plasma code of Kaastra & Mewe (1993; incorporating the Fe L calculations by Liedhal) was again used.

Column 5 of Table 3 lists the best-fitting temperatures (for the ambient cluster gas) and 90 per cent ($\Delta\chi^2 = 2.71$) confidence limits for the clusters. The spectrally determined mass deposition rates and intrinsic X-ray absorbing column densities are listed in columns 6 and 7 of that Table.

3.2 X-ray imaging analysis and mass results

The analysis of the HRI imaging data was carried out using an updated version of the deprojection code of Fabian et al. (1981; see also White et al. 1997 for details). Azimuthally averaged X-ray surface brightness profiles were determined for each cluster from the HRI images. The profiles were background-subtracted, corrected for telescope vignetting and re-binned to provide sufficient counts in each radial bin for the deprojection analysis to be successfully carried out (bin sizes of 8–24 arcsec were used).

With the X-ray surface brightness profiles as the primary input, and under assumptions of spherical symmetry and hydrostatic equilibrium in the ICM, the deprojection technique can be used to study the basic properties of the intracluster gas (temperature, density, pressure, cooling rate) as a function of radius. The code uses a Monte Carlo method to determine the statistical uncertainties on the results and incorporates the latest HRI spectral response matrix issued by GSFC. The metallicity and absorbing column density of the cluster gas were fixed at the values determined from the spectral analysis in Section 3.1.

The deprojection code requires the total mass profiles for the clusters (which define the pressure profiles) to be specified. We have iteratively determined the mass profiles that result in deprojected temperature profiles (which approximate the mass-weighted temperature profiles in the clusters) that are isothermal within the regions probed by the HRI data (the central $0.5 - 1$ Mpc) and which are consistent with the spectrally-determined temperatures from Section 3.1. The assumption of approximately isothermal mass-weighted temperature profiles in the central regions of the clusters is supported by the following evidence: first, *ASCA* observations of nearby cooling flows show that in the central regions of these systems the gas is multiphase, but that the bulk of the X-ray gas there has a temperature close to the cluster mean (e.g. Fukazawa et al. 1994; Ohashi et al. 1997; Allen et al., in preparation). Secondly, the combined X-ray and gravitational lensing studies of the cooling-flow clusters PKS0745−191 and Abell 1835 (Allen et al. 1996a,b) demonstrated that approximately isothermal mass-weighted temperature profiles are required to consistently explain the X-ray imaging and spectral data for these systems, and result in good agreement between the X-ray and gravitational-lensing masses for the clusters. Thirdly, the use of approximately constant mass-weighted temperature profiles implies a more plausible range of initial density inhomogeneities in the clusters than would be the case if the temperature profiles decreased within the cluster cores (Thomas, Fabian & Nulsen 1987). Finally, the use of approximately isothermal mass-weighted temperature profiles in the deprojection analyses leads to independent determinations of the mass deposition profiles for the cooling flows, from the X-ray spectra and imaging data, in excellent agreement with each other (Allen & Fabian 1997). We note that the assumption of a constant mass-weighted temperature profile is consistent with measurements of decreasing emission-weighted temperatures in the cores of cooling-flow clusters (Waxman & Miralda-Escudé 1995).

The mass profiles for the clusters were parametrized as isothermal spheres (equation 4-125 of Binney & Tremaine 1987) with adjustable core radii, r_c, and velocity dispersions, σ. The core radii were adjusted until the temperature profiles determined from the deprojection code became isothermal. The velocity dispersions were then adjusted until the temperatures determined from the deprojection code came into agreement with the spectrally determined values. Errors on the velocity dispersions are the range of values that result in isothermal deprojected temperature profiles that are consistent, at the 90 per cent confidence limit, with the spectrally determined temperatures. Errors on the core radii

Table 4. Strong lensing and X-ray mass measurements.

	LENSING			X-RAY			RATIO
	r_{arc} (kpc)	z_{arc}	M_{arc} (10^{13} $M_\odot$)	σ (km s^{-1})	r_c (kpc)	M_X (10^{13} $M_\odot$)	M_{arc}/M_X
COOLING FLOWS							
PKS0745-191	45.9	0.433	2.99	930^{+90}_{-70}	37.5(±5)	$3.16^{+0.64}_{-0.46}$	$0.95^{+0.16}_{-0.16}$
RXJ1347.5-1145	240	1.00 (2.00)	51.0 (35.8)	1850^{+270}_{-500}	75(±15)	$68.1^{+21.4}_{-31.8}$	$0.75^{+0.65}_{-0.18}$ $(0.53^{+0.46}_{-0.13})$
MS1358.4+6245	121	4.92	8.27	830^{+340}_{-80}	40(±30)	$7.03^{+6.97}_{-1.29}$	$1.18^{+0.26}_{-0.59}$
Abell 1835	150	1.00 (2.00)	18.1 (15.4)	1000^{+120}_{-70}	50(±20)	$12.6^{+3.2}_{-1.7}$	$1.44^{+0.22}_{-0.29}$ $(1.22^{+0.19}_{-0.25})$
Abell 2390	174	0.913	25.4	1190^{+520}_{-240}	60(±20)	$21.2^{+22.6}_{-7.7}$	$1.20^{+0.68}_{-0.62}$
MS2137.3-2353	88.0	1.00 (2.00)	6.15 (4.98)	830^{+140}_{-50}	32(±25)	$5.19^{+1.88}_{-0.62}$	$1.18^{+0.17}_{-0.31}$ $(0.96^{+0.13}_{-0.26})$
INTERMEDIATE							
Abell 963	79.8	0.771	5.85	750^{+50}_{-50}	80(±25)	$3.29^{+0.47}_{-0.41}$	$1.78^{+0.25}_{-0.22}$
Abell 1689	183	1.00 (2.00)	29.5 (26.4)	990^{+60}_{-50}	80(±15)	$15.3^{+2.0}_{-1.5}$	$1.93^{+0.21}_{-0.22}$ $(1.73^{+0.18}_{-0.20})$
NON COOLING-FLOWS							
Abell 2744(2)	119.6	1.00 (2.00)	11.36 (9.23)	930^{+60}_{-50}	450	$2.78^{+0.37}_{-0.29}$	$4.09^{+0.47}_{-0.48}$ $(3.32^{+0.39}_{-0.39})$
Abell 2163	67.7	0.73	4.29	1050^{+50}_{-50}	300	$1.74^{+0.17}_{-0.16}$	$2.47^{+0.25}_{-0.22}$
Abell 2218(#359)	79.4	0.702	6.23	830^{+30}_{-40}	230	$1.89^{+0.14}_{-0.18}$	$3.30^{+0.34}_{-0.23}$
Abell 2218(#384)	84.8	2.515	5.70	830^{+30}_{-40}	230	$2.14^{+0.16}_{-0.20}$	$2.66^{+0.28}_{-0.18}$
*Abell 2219N	79.3	1.00 (2.00)	5.17 (4.48)	950^{+50}_{-50}	250	$2.59^{+0.25}_{-0.32}$	$2.00^{+0.28}_{-0.18}$ $(1.73^{+0.24}_{-0.15})$
*Abell 2219L	110.2	1.00 (2.00)	9.98 (8.65)	950^{+50}_{-50}	250	$4.53^{+0.45}_{-0.60}$	$2.20^{+0.34}_{-0.20}$ $(1.91^{+0.29}_{-0.17})$
AC114 (S1+D1/S2+D2)	67.6	1.86	2.98	910^{+80}_{-70}	300	$1.30^{+0.24}_{-0.19}$	$2.29^{+0.39}_{-0.35}$

Notes: The masses within the arc radii determined from the spherically symmetric strong-lensing analyses (Section 3.3) and X-ray modelling (Sections 3.1, 3.2). Errors on the X-ray masses and the strong-lensing to X-ray mass ratios are 90 per cent confidence limits. No statistical error has been associated with the lensing masses. (For an estimate of the systematic uncertainties associated with the lensing results see the discussion of the analyses with the more detailed lensing models, Section 4.3). References for the lensing data are as follows: details for PKS0745-191 from Allen et al. (1996a). RXJ1347.7–1145 arc radius from Schindler et al. (1997). MS1358.4+6245 arc radius and redshift from Franx et al. (1997). Abell 1835 arc radius from Edge et al. (in preparation). MS2137-2353 arc radius from Fort et al. (1992). Abell 2390 arc radius and redshift from Pelló et al. (1991). Lensing details for Abell 1689 and Abell 2163 from Miralda-Escudé & Babul (1995) and references therein. Abell 963 arc radius from Lavery & Henry (1988) and redshift from Ellis et al. (1992). Abell 2744 (AC118) arc radius from Smail et al. (1991). Arc radii for Abell 2218 from Kneib et al. (1995). Redshift for arc #359 from Pelló et al. (1992). Redshift for arc #384 from Ebbels et al. (1996). Arc radii for Abell 2219 from Smail et al. (1995a). Arc radius and redshift for AC114 from Smail et al. (1995b). For Abell 2218 and 2219, we determine mean (unweighted) M_{arc}/M_X values from the two brightest arcs in these clusters of 3.0 and 2.1 (1.8), respectively.

* The X-ray-determined mass model for Abell 2219 includes a 3×10^{12} $M_\odot$ singular isothermal sphere truncated at 30 kpc, which improved the isothermality of the deprojected temperature profile.

denote the range of values that are consistent with isothermality in the deprojected temperature profiles. Errors on the core radii are only listed for the cooling-flow and intermediate clusters since, for the non-cooling flow systems, the large core radii inferred are likely to be due to recent merger events having disrupted the central regions of the clusters, invalidating the assumption of hydrostatic equilibrium (Sections 4.4, 4.6). [We note that an initial estimate for the pressure in the outermost radial bin used in the analysis is also required by the deprojection code. These values were also determined iteratively, under the assumption of isothermality. The uncertainties on these pressure estimates do not significantly affect the results presented here. Note also that the core radii determined from the deprojection analysis are similar, though not identical, to the values determined from simple 'β-model' fits to the X-ray surface brightness profiles, e.g. Jones & Forman 1984.]. The mass distributions determined from the deprojection analysis are summarized in columns 5 and 6 of Table 4. In column 7 we list the projected masses, inferred from these distributions, within the critical radii defined by the gravitational arcs in the clusters (Section 3.3). The mass distributions are assumed to extend to radii of 3 Mpc.

Finally, we note that although the deprojection method of Fabian et al. (1981) is essentially a single-phase technique, it produces results in good agreement with more detailed multiphase treatments

(Thomas et al. 1987) and, because of its simple applicability at large radii in clusters, is better suited to the present project. Detailed results on the cooling flows in these clusters, also determined from the deprojection code, are presented by Allen et al. (in preparation).

3.3 Strong gravitational lensing analysis

The lensing data used in this paper have been drawn from the literature and are summarized in Table 4 (columns 2 and 3, with references listed in the caption). The X-ray modelling presented in Sections 3.1 and 3.2 was carried out under the assumption of spherical symmetry in the cluster mass distributions. The use of a spherically symmetric geometry in the X-ray analyses, where the underlying cluster mass distributions are ellipsoidal, will tend to slightly overestimate the X-ray gas pressure and, therefore, the gravitating mass as a function of radius. However, the use of spherical models is not unreasonable since the X-ray gas (in hydrostatic equilibrium) will trace the cluster potentials, which will be more spherical than the mass distributions, particularly at large radii. The spherical analysis also avoids degeneracies associated with the unknown oblate/prolate nature of the mass distributions. The X-ray masses determined with the spherical modelling should be accurate to $\lesssim10$ per cent (e.g. Buote & Tsai 1996a).
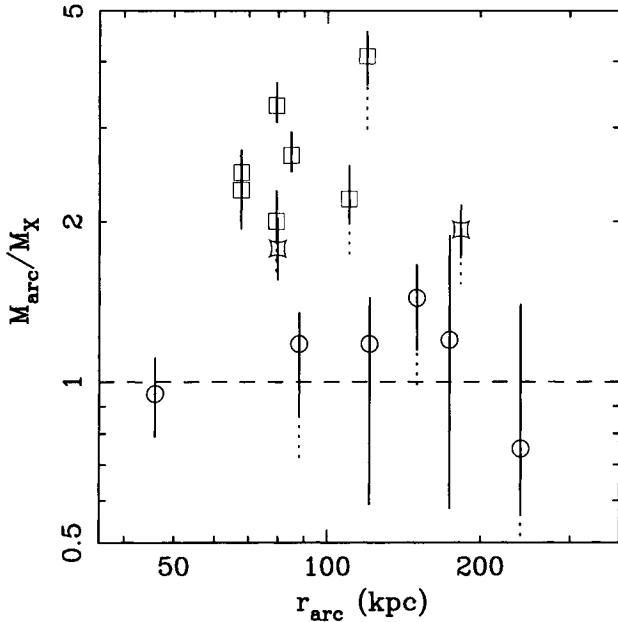
Figure 1. The ratio of the strong-lensing to X-ray mass measurements as a function of the arc radius (as detailed in Table 4). The measurements for the cooling-flow clusters are plotted as circles. The non-cooling systems are plotted as squares. The two intermediate systems (Abell 963 and Abell 1689) are indicated by pinched squares. The solid error bars denote the 90 per cent confidence limits on the mass ratios, given the redshift of the arc (where known) or for an assumed arc redshift, $z_{arc} = 1.00$. Dotted error bars (where plotted) denote the confidence limits for an assumed arc redshift of $z_{arc} = 2.00$. For the cooling-flow clusters, good agreement between the strong-lensing and X-ray mass measurements is observed. For the non-cooling flow systems, the lensing mass exceeds the X-ray mass by a factor of 2–4. For the two intermediate clusters the lensing mass exceeds the X-ray determined value by a smaller factor of 1.7–2.0. The origins of the discrepancies between the strong-lensing and X-ray masses for the non-cooling flow clusters are explored in Section 4.

In the first case, for simplicity and to be consistent with the X-ray analysis, we have carried out a basic lensing analysis using circularly symmetric models for the lensing potentials. As will be shown in Section 4.3, the use of more realistic, elliptical mass models can reduce the masses within the arc radii by up to 40 per cent, although values of ~20 per cent are more typical (see also Bartelmann 1995). However, such corrections are not significant in comparison to the factor $\gtrsim 2$ discrepancies between the X-ray and lensing masses reported for clusters like Abell 1689 and 2218 (Miralda-Escudé & Babul 1995).

For a circular mass distribution the projected mass within the tangential critical radius, assumed to be equal to the arc radius, r_{arc}, is given by

$$M_{arc}(r_{arc}) = \frac{c^2}{4G} \left(\frac{D_{arc}}{D_{clus} D_{arc-clus}} \right) r_{arc}^2 \qquad (1)$$

where D_{clus}, D_{arc} and $D_{arc-clus}$ are respectively the angular diameter distances from the observer to the cluster, the observer to the lensed object, and the cluster to the lensed object. (We note that where the lensed features do not lie exactly on the critical curves, small overestimates of the lensing masses are likely to result). Where redshifts for the arcs are not available, we calculate masses for assumed arc redshifts of 1.00 and 2.00. The masses within the arc radii, determined from the lensing analysis, are summarized in Table 4 (column 4).

4 RESULTS AND DISCUSSION

4.1 The ratio of strong-lensing to X-ray masses

The ratios of the mass measurements from the strong-lensing (Section 3.3) and X-ray (Sections 3.1, 3.2) data are listed in Table 4 (column 8). Fig. 1 shows the ratios of the lensing and X-ray masses as a function of arc radius. The results demonstrate a clear segregation between the cooling-flow and non-cooling flow systems.

All of the cooling-flow clusters in our sample exhibit good agreement between their X-ray and strong-lensing masses. In particular, for those clusters with measured arc redshifts, excellent agreement between the X-ray and strong-lensing masses is observed. For the non-cooling flows, the strong-lensing masses exceed the X-ray masses by factors of 2–4. For the two intermediate systems, where the detections of cooling flows from the X-ray data are more marginal, the lensing masses are again enhanced with respect to the X-ray values, although by a smaller factor (1.7 − 2.0). We find excellent agreement with the results of Miralda-Escudé & Babul (1995) for the three (non-cooling flow) clusters in common with that study; Abell 1689, 2163 and 2218.

Our results support the conclusions drawn by Allen et al. (1996a,b) that thermal pressure dominates over magnetic pressure, turbulence and bulk motions in the central regions of the relaxed cooling-flow clusters, and that the hydrostatic assumption adopted in the X-ray analysis of such systems is valid. In all cases in which discrepancies between the X-ray and strong-lensing masses occur, the clusters appear dynamically active and have either small (in comparison to their total X-ray luminosities) or no cooling flows. Clusters like Abell 1689, AC114, Abell 2163 and Abell 2218 have unusually high velocity dispersions (Gudehus 1989; Couch & Sharples 1987; Squires et al. 1997a; Le Borgne, Pelló & Sanahuja 1992), given their X-ray luminosities, and exhibit clear substructure in their X-ray emission, galaxy distributions and total matter distributions (see also Section 4.3 and references therein). Merger events will tend to complicate the temperature structure in clusters, and generate turbulent and bulk motions which may contribute to the support of the X-ray gas against gravity. Although the discrepancies between the X-ray and strong-lensing masses resulting from such processes should not, in general, exceed 50 per cent (Navarro, Frenk & White 1995; Schindler 1996; Evrard, Metzler & Navarro 1996; Roettiger, Burns & Loken 1996), at smaller radii (comparable to the cluster core radii) their effects may be more important (see Section 4.6).

Substructure and line-of-sight alignments of material towards the cluster cores are also likely to contribute to the mass discrepancies since they will increase the probability of detecting gravitational arcs in the clusters, and enhance the masses determined from the lensing data (Bartelmann & Steinmetz 1996). However, since magnetic fields are expected to be stronger in the cores of cooling-flow, rather than non-cooling flow, systems (e.g. Soker & Sarazin 1990), magnetic pressure seems unlikely to contribute significantly to the differences between the strong-lensing and X-ray masses observed.

4.2 The effects of cooling flows on the X-ray data

The results presented in Section 4.1 demonstrate excellent agreement between the X-ray and strong-lensing masses for the cooling-flow clusters in our sample. It is crucial to note, however, that such agreement would not have been obtained if the multiphase nature of

Table 5. The effects of cooling flows on the X-ray masses.

	ΔkT (keV)	M_X (10^{13} $M_\odot$)	$M_{X,I}$ (10^{13} $M_\odot$)	RATIO ($M_X/M_{X,I}$)
COOLING FLOWS				
PKS0745-191	$2.2^{+1.8}_{-1.4}$	$3.16^{+0.64}_{-0.46}$	$2.34^{+0.11}_{-0.12}$	$1.35^{+0.36}_{-0.25}$
RXJ1347.5-1145	$16.0^{+8.6}_{-13.2}$	$68.1^{+21.4}_{-31.8}$	$27.0^{+2.1}_{-2.1}$	$2.52^{+0.79}_{-1.27}$
MS1358.4+6245	$1.8^{+7.7}_{-2.3}$	$7.03^{+6.97}_{-1.29}$	$5.44^{+0.77}_{-0.58}$	$1.29^{+1.59}_{-0.37}$
Abell 1835	$2.5^{+2.6}_{-1.7}$	$12.6^{+3.2}_{-1.7}$	$9.13^{+0.65}_{-0.43}$	$1.38^{+0.44}_{-0.27}$
MS2137.3-2353	$0.8^{+2.2}_{-1.2}$	$5.19^{+1.88}_{-0.62}$	$4.46^{+0.35}_{-0.46}$	$1.16^{+0.61}_{-0.21}$
Abell 2390	$5.6^{+16.5}_{-6.5}$	$21.2^{+22.6}_{-7.7}$	$13.1^{+1.7}_{-1.6}$	$1.62^{+2.19}_{-0.71}$
INTERMEDIATE				
Abell 963	—	$3.29^{+0.47}_{-0.41}$	$3.29^{+0.27}_{-0.17}$	$1.00^{+0.21}_{-0.19}$
Abell 1689	$0.8^{+1.6}_{-1.2}$	$15.3^{+2.0}_{-1.5}$	$14.0^{+0.8}_{-0.6}$	$1.10^{+0.19}_{-0.17}$

Notes: The differences between the temperatures and masses determined from the X-ray analyses with the cooling-flow and isothermal spectral models. The errors on the masses (M_X and $M_{X,I}$ respectively) are 90 per cent confidence limits. The errors on the temperature differences (ΔkT) and mass ratios ($M_X/M_{X,I}$) mark the maximum and minimum values consistent with the joint 90 per cent confidence limits on the results obtained with cooling flow and isothermal models.

the X-ray emission from these clusters were not accounted for in the X-ray modelling.

The analysis of the *ASCA* data for the cooling-flow (and intermediate) clusters in Section 3.1 incorporated a cooling-flow component (with intrinsic absorption) in the spectral modelling. The cooling-flow component accounts for the spectral signature from material cooling out of the X-ray waveband from the ambient cluster temperature. The luminosity of this component, which is a free parameter in the fits, is generally found to be in excellent agreement with the cooling rates determined independently from the deprojection analysis of the imaging data (Allen et al., in preparation), lending strong support to the validity of this model. If the cooling-flow component were not incorporated into the spectral analysis, and a more simple isothermal spectral model were inappropriately used instead, the measured temperatures would significantly underestimate the 'true' values listed in Table 3.

The differences between the temperatures determined using the models incorporating the cooling-flow components and the results obtained using the more simple isothermal spectral models are summarized in Table 5. Also listed in that table are the total masses within the arc radii determined with the cooling-flow (M_X; as in Table 4) and isothermal ($M_{X,I}$) spectral models, and the ratios of these values ($M_X/M_{X,I}$). We see that failure to account for complexities in the X-ray spectra arising from the presence of cooling flows will typically result in underestimates of the cluster masses by 10 − 40 per cent. For RXJ1347.5-1145, the hottest and most X-ray luminous cluster in our sample, the underestimation is even more severe; a factor of 2−3. This is primarily a result of the difficulty in constraining the temperatures of the hottest clusters ($kT \gtrsim 10$ keV) using the 0.6−10.0 keV bandpass of *ASCA*. Such effects completely account for the discrepancy between the X-ray and strong-lensing masses for RXJ1347.5-1145 reported by Schindler et al. (1997). [We note that exact agreement between the strong-lensing and X-ray masses for RXJ1347.5-1145 is achieved for an X-ray temperature of $kT \sim 19(13.5)$ keV, for an assumed redshift for the arc of 1.00 (2.00), which is consistent with our spectral constraints.] The two intermediate clusters in our sample, Abell 963 and Abell 1689, have lower fractions of their
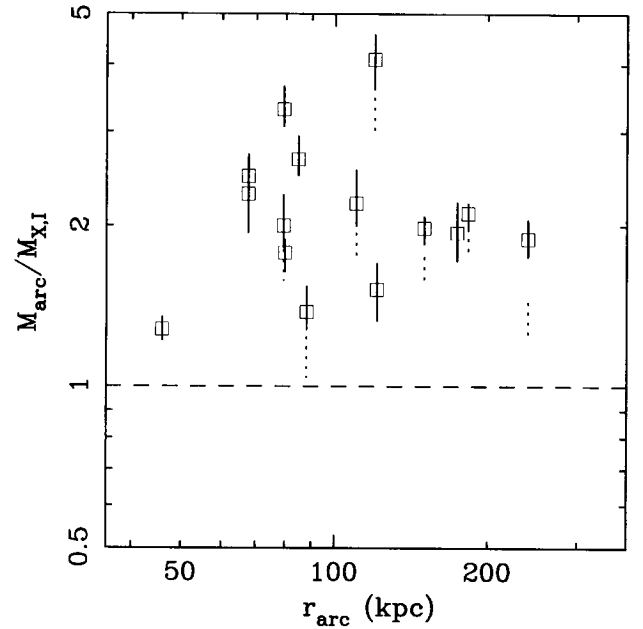

Figure 2. The ratio of the strong-lensing to X-ray mass as a function of the arc radius (determined with the spherically symmetric lensing models) when no account is taken of the effects of cooling flows on the X-ray data. Simple, isothermal X-ray spectral models have been used for all clusters, including the cooling-flow systems. This figure (and comparison to Fig. 1) illustrates how the failure to account for the presence of cooling flows in the X-ray analyses can lead to the false conclusion that the strong-lensing mass invariably exceeds the X-ray determined mass, even in the relaxed cooling-flow systems.

X-ray luminosities contributed by their cooling flows (Allen et al., in preparation) and the errors incurred by not accounting for the effects of the cooling flows on their X-ray determined masses are therefore less severe.

These results are shown in graphical form in Fig. 2, where we plot the ratios of the strong-lensing and X-ray masses, determined with the isothermal models, as a function of the arc radius. We see that for all clusters $M_{arc} > M_{X,I}$. (Note that for the non-cooling flow clusters $M_{X,I} = M_X$ in Table 4). This figure, together with Fig. 1, clearly illustrates how the failure to account for the presence of cooling flows in the X-ray analyses can lead to the incorrect conclusion that the strong-lensing mass invariably exceeds the X-ray determined mass.

Finally, in this section, we note that our analysis of the non-cooling flow clusters was carried out with the absorbing column density included as a free parameter in the spectral fits. Column densities in excess of the Galactic values were statistically required for Abell 2744, 2163 and 2219 and for AC114 (Allen et al., in preparation). With the column densities fixed at nominal Galactic values (Dickey & Lockman 1990), the measured temperatures were somewhat higher; $kT = 11.0^{+0.8}_{-0.7}$, $13.8^{+0.8}_{-0.7}$, $12.4^{+0.8}_{-0.7}$ and $9.8^{+1.0}_{-0.9}$ keV for Abell 2744, 2163, 2219 and AC114, respectively. The corresponding X-ray masses within the arc radii are then 4.1×10^{13} for Abell 2744, 2.3×10^{13} for Abell 2163, 3.1×10^{13} and 5.5×10^{13} $M_\odot$ for the N and L arcs of Abell 2219, and 1.7×10^{13} for AC114. The ratios of the strong-lensing to X-ray masses are reduced to 2.8 (2.2) for Abell 2744, 1.9 for Abell 2163, 1.7 (1.4) and 1.8 (1.6) for the N and L arcs in Abell 2219, and 1.8 for AC114. Although the temperature results are therefore sensitive, in detail, to the modelling of the absorbing column density, the differences are not

enough to account for the discrepancies between the strong-lensing and X-ray mass measurements for the non-cooling flow clusters.

4.3 More detailed lensing models

Several of the clusters discussed in this paper are well-studied lensing systems. From their detailed study of Abell 2218, Kneib et al. (1995) demonstrated that the observed arc(let) configuration implies a mass distribution consisting of two clumps centred on the two brightest galaxies. The orientation and ellipticities of the projected potentials due to these clumps trace the external isophotes of brightest ellipticals. [Similar results on the orientation of the dark matter potentials relative to the isophotes of the dominant cluster galaxies were obtained from the lensing studies of MS2137.3−2353 and Abell 370 by Mellier, Fort & Kneib (1993) and Kneib et al. (1993). These results may be compared to similar findings based on the galaxy and X-ray gas distributions in other clusters, e.g. Porter, Schneider & Hoessel (1991), Allen et al. (1995).] The lensing results on Abell 2218, and comparison to a *ROSAT* HRI X-ray image of the cluster (from a shorter 11.5 ks exposure) lead Kneib et al. (1995) to suggest that Abell 2218 is undergoing a subcluster merger event, which may have shocked the central X-ray gas and caused it to deviate from hydrostatic equilibrium. From their modelling, Kneib et al. (1995) determine a mass within the ellipse traced by arc number 384 of 6.1×10^{13} M$_\odot$, similar to the value of 5.7×10^{13} M$_\odot$ inferred from the simple spherical model. Miralda-Escudé & Babul (1995) showed that the application of a multi-component lensing model, which can account for the positions of the brightest arcs in Abell 2218, predicts a lensing mass within the circular aperture defined by arc number 359 of ∼87 per cent of the value inferred from the simple spherical model. This implies $M_{arc}/M_X = 2.87^{+0.30}_{-0.20}$, which is again similar to the result listed in Table 4. (Recall that the errors quoted on the M_{arc}/M_X values denote the largest and smallest values consistent with the joint confidence limits on the X-ray masses and lensing results).

From their detailed lensing analysis of the cooling-flow cluster MS2137.3−2353, Mellier et al. (1993) determined a mass within the external critical radius of $M_{arc} = 3 - 7 \times 10^{13}$ M$_\odot$. This is consistent with the value determined from the circularly symmetric model and is in excellent agreement with the X-ray-determined mass measurement of $M_X = 5.2^{+1.9}_{-0.6} \times 10^{13}$ M$_\odot$ (implying $M_{arc}/M_X = 0.96^{+0.56}_{-0.54}$). Mellier et al. (1993) also concluded that the core radius of the lensing potential in MS2137.3−2353 is small (∼50 kpc), in good agreement with the X-ray result reported here (see also Section 4.6).

For Abell 1689, Miralda-Escudé & Babul (1995) showed that the application of a mass model consisting of (at least) two clumps is required to reproduce the positions of the brightest arcs. The mass within the circular aperture defined by the dominant arc, determined with their model, is slightly larger (104 per cent) than the value inferred from the simple spherical model, and gives $M_{arc}/M_X = 2.00^{+0.22}_{-0.23}$ ($1.80^{+0.19}_{-0.21}$).

Smail et al. (1995a) present results from a detailed lensing analysis of Abell 2219 using a multi-component mass model. These authors determine a projected mass within 100 kpc of the cluster centre of $1.1 \pm 0.2 \times 10^{14}$ M$_\odot$, in reasonable agreement with (although slightly larger than) the values suggested by the simple spherically symmetric model (Table 4). The X-ray-determined mass within this projected radius is $3.54^{+0.38}_{-0.51} \times 10^{13}$ M$_\odot$, implying a strong-lensing/X-ray mass ratio of $M_{arc}/M_X = 3.11^{+1.18}_{-0.81}$. Smail et al. (1995a) also infer a core radius for the dominant mass clump of 46 ± 20 kpc.

Allen et al. (1996a) present results from a more detailed lensing analysis of PKS0745−191. These authors show that the application of an elliptical potential leads to a projected mass within the arc radius of $2.5^{+0.2}_{-0.4} \times 10^{13}$ M$_\odot$, approximately 20 per cent lower than the value inferred from the spherical model. The implied M_{arc}/M_X value is then $0.79^{+0.21}_{-0.22}$. The lensing data for PKS0745−191 also suggest a small core radius of ∼40 kpc, in good agreement with the value inferred from the X-ray analysis.

Pierre et al. (1996) present a more sophisticated lensing analysis of the cooling-flow cluster Abell 2390 (employing a two-component lensing model). These authors determine a projected mass within the arc radius of $1.6 \pm 0.2 \times 10^{14}$ M$_\odot$. This value is ∼40 per cent lower than the value determined from the simple, circular lensing model, but is in good agreement with the X-ray measurement of $M_X = 2.1^{+2.3}_{-0.8} \times 10^{14}$ M$_\odot$ reported here, and implies $M_{arc}/M_X = 0.76^{+0.62}_{-0.44}$. Pierre et al. (1996) adopt a core radius for the mass distribution of the dominant clump in their lensing model of 60 kpc, identical to that inferred from the X-ray analysis.

Natarajan et al. (1997) present results from a detailed analysis of lensing data for AC114. These authors determine masses within radii of 75, 150 and 500 kpc of the cluster centre of $4.2 \pm 0.1 \times 10^{13}$, $1.20 \pm 0.15 \times 10^{14}$, and $4.0 \pm 0.4 \times 10^{14}$ M$_\odot$, respectively. These measurements compare to X-ray determined values within the same radii of $1.59^{+0.30}_{-0.23} \times 10^{13}$, $5.82^{+1.07}_{-0.86} \times 10^{13}$, and $3.40^{+0.63}_{-0.50} \times 10^{14}$ M$_\odot$. This implied lensing/X-ray mass ratios at these radii are then $2.64^{+0.52}_{-0.47}$, $2.06^{+0.66}_{-0.56}$, and $1.18^{+0.34}_{-0.29}$, respectively. The Natarajan et al. (1997) value at 75 kpc is similar to that listed in Table 4.

In conclusion, we see that although the more detailed lensing analyses refine the results on the strong-lensing/X-ray mass ratios, the conclusions drawn from Section 4.1, using the simple spherically symmetric lensing models, remain essentially unchanged. The M_{arc}/M_X ratios for cooling-flow clusters (the more dynamically relaxed systems) show excellent agreement. For the non-cooling flow clusters, the masses inferred from the strong-lensing data are ∼2 − 4 times larger than the X-ray measurements. We shall now explore the reasons for this discrepancy.

4.4 Offsets between the lensing and X-ray centres in non-cooling-flow clusters

The X-ray emission from a cooling-flow cluster is typically regular (with an approximately ellipsoidal symmetry) and sharply peaked on to a position co-incident with, or close to, the position of the optically dominant cluster galaxy (e.g. Allen et al. 1995; Allen et al. 1996b). In such clusters, the X-ray gas and arc(let)s should trace the same cluster potential. In non-cooling flow systems, however, the situation is less clear. Clusters without cooling flows generally exhibit more substructure in their X-ray images (Buote & Tsai 1996b) and appear more complex in their galaxy and dark matter distributions. Such clusters are often inferred to be undergoing major subcluster merger events. Non-cooling flow clusters do not have a sharply defined peak to their X-ray emission in the same manner that cooling-flow clusters do (cf. Section 2). Thus, although detailed lensing studies show that the arc(let) configurations in such clusters are still typically centred on the dominant cluster galaxies (non-cooling flow clusters often have more than a single dominant galaxy), these galaxies are not necessarily coincident with the centres of the X-ray emission from the clusters. In such circumstances, simple comparisons of X-ray and strong-lensing mass measurements, such as those presented in Sections 4.1−4.3, may not be applicable.

Table 6. Offsets between the X-ray and lensing centroids.

	Lensing Centre R.A. (J2000.)	Dec. (J2000.)	Offset (arcsec)	(kpc)	r_{arc} (kpc)
COOLING FLOWS					
PKS0745-191	$07^h47^m31.3^s$	$-19°17'41''$	6.6	16.6	45.9
RXJ1347.5-1145	$13^h47^m30.7^s$	$-11°45'11''$	4.4	30.0	240
MS1358.4+6245	$13^h59^m50.7^s$	$62°31'05''$	0.7	4.0	121
Abell 1835	$14^h01^m02.2^s$	$02°52'40''$	3.0	14.8	150
MS2137.3-2353	$21^h40^m15.3^s$	$-23°39'41''$	1.4	7.9	88.0
Abell 2390	$21^h53^m36.9^s$	$17°41'43''$	6.1	28.6	174
INTERMEDIATE					
Abell 963	$10^h17^m03.8^s$	$39°02'47''$	6.1	26.3	79.8
Abell 1689	$13^h11^m29.6^s$	$-01°20'29''$	13.3	52.9	183
NON COOLING FLOWS					
Abell 2744	$00^h14^m20.8^s$	$-30°24'03''$	58.7	328	119.6
Abell 2163	$16^h15^m49.1^s$	$-06°08'43''$	50.0	217	67.7
Abell 2218	$16^h35^m49.5^s$	$66°12'43''$	22.9	87.8	79.4/84.8
Abell 2219	$16^h40^m19.8^s$	$46°42'41''$	12.7	58.7	79.3/110.2
AC114	$22^h58^m48.4^s$	$-34°48'10''$	9.7	54.6	67.6

Notes: The lensing centres and offsets (in arcsec and kpc) with respect to the X-ray centres listed in Table 2. For comparison, the arc radii, within which the strong-lensing masses are evaluated, are also listed. For Abell 2218 and 2219 the radii for both of the two brightest arcs are given.

We have examined the alignment of the X-ray centroids (Table 2) with the centroids of the matter distributions inferred from the lensing studies (which are defined as the optical centres of the dominant cluster galaxies around which the arc(let)s are observed). The galaxy positions were measured from the Space Telescope Science Institute Digitized Sky Survey (hereafter DSS). In Table 6 we list the DSS coordinates for the relevant galaxies and the separations (in arcsec and kpc) between the lensing and X-ray centroids. The accuracy of the optical and X-ray coordinates are such that offsets between these positions of >10 arcsec should be considered significant (cf. David et al. 1996).

The results listed in Table 6 show that for all of the cooling-flow clusters, the X-ray and lensing centres are consistent with each other, in agreement with previous results (e.g. Allen et al. 1995). For the non-cooling-flow systems, however, significant offsets between the X-ray and lensing centres are observed. In all cases, the sizes of these offsets are comparable to or larger than the radii at which the arcs are observed. We note that an offset of ~20 arcsec between the X-ray centroid and the dominant galaxy in Abell 2218 was previously noted by Markevitch (1997). Our results show that the X-ray and lensing mass measurements discussed in Sections 4.1–4.3 are actually probing different lines of sight through the clusters and, therefore, that direct comparisons of these values are not strictly valid.

Within the context of stable, spherically symmetric mass models, the projected mass through a region of fixed radius, centred on any position other than the cluster centre, will always be less than the mass through the centre. Thus the discrepancies between the X-ray and lensing masses are not immediately explained by the offsets between the X-ray and lensing centres. However, the results on the offsets show that the X-ray gas in the central regions of the non-cooling flow clusters is not in hydrostatic equilibrium with the gravitational potentials inferred from the lensing data. In Section 4.6 we shall show how the breakdown of the hydrostatic assumption can lead the X-ray measurements to significantly underestimate the true cluster masses.

4.5 A comparison with weak-lensing results

A number of the clusters discussed in this paper have also been the subject of detailed weak-lensing analyses. Studies of weak lensing by clusters of galaxies probe the projected matter distributions on spatial scales ~1 Mpc, significantly larger than the offsets between the X-ray and lensing centres determined for the non-cooling flow clusters (Section 4.4).

From their study of Abell 2218, Squires et al. (1996) determine a lower bound to the mass within an 800 kpc (3.5 arcmin) radius of the cluster centre of $7.8 \pm 1.4 \times 10^{14}$ $M_\odot$. This compares to an X-ray-determined mass within the same region of $4.31^{+0.32}_{-0.40} \times 10^{14}$ $M_\odot$. The Squires et al. (1996) weak-lensing mass thus exceeds the X-ray determined value for the central 800 kpc by a factor ~1.8. Within a smaller 400 kpc (radius) region, however, Squires et al. (1996) determine a mass of $2.4 \pm 0.6 \times 10^{14}$ $M_\odot$ (this value has been estimated from their fig. 16) in good agreement with the X-ray measurement of $2.29^{+0.17}_{-0.22} \times 10^{14}$ $M_\odot$ from the analysis presented here. Smail et al. (1997) also present results from a weak-lensing study of *HST* images of Abell 2218 from which they measure a mass within the central 400 kpc (radius) region of the cluster of $2.10 \pm 0.38 \times 10^{14}$ $M_\odot$, in excellent agreement with the Squires et al. (1996) and X-ray results. The weak-lensing results for Abell 2218 thus suggest an unusual (non-isothermal) projected mass profile between radii of 400 and 800 kpc with a density gradient flatter than r^{-1}. We note that the weak-lensing mass for Abell 2218 within 800 kpc (Squires et al. 1996) appears high, given that this mass is comparable to the value determined for Abell 2390 within a similar aperture (see below), despite the fact that the 2 − 10 keV X-ray luminosity of Abell 2390 is ~4 times higher than that of Abell 2218. Such conclusions are not significantly affected by the remodelling of the X-ray mass profiles with smaller core radii discussed in Section 4.6.

From their weak-lensing study of Abell 2163, Squires et al. (1997a) determine (from their fig. 5) a mass within a 200-arcsec (870 kpc) radius aperture of $\sim 5 \times 10^{14}$ $M_\odot$ (with a factor ~2

Table 7. Weak lensing and X-ray mass measurements.

	r_{weak} (kpc)	M_{weak} (10^{13} $M_\odot$)	$M_{\text{X,weak}}$ (10^{13} $M_\odot$)	RATIO ($M_{\text{weak}}/M_{\text{X,weak}}$)
COOLING FLOWS				
RXJ1347.5-1145	2000	340 ± 80	360^{+110}_{-170}	$0.94^{+1.27}_{-0.39}$
Abell 2390	940	100 ± 40	82^{+87}_{-30}	$1.22^{+1.47}_{-0.86}$
NON COOLING FLOWS				
Abell 2744	400	37.0 ± 6.4	$23.3^{+3.1}_{-2.4}$	$1.59^{+0.49}_{-0.43}$
Abell 2163	870	50 ± 25	$76.3^{+7.5}_{-7.0}$	$0.66^{+0.42}_{-0.36}$
Abell 2218(a)	800	78 ± 14	$43.1^{+3.2}_{-4.0}$	$1.81^{+0.54}_{-0.43}$
Abell 2218(b)	400	21.0 ± 3.8	$22.9^{+1.7}_{-2.2}$	$0.92^{+0.28}_{-0.22}$
AC114	500	40 ± 4	$34.0^{+6.2}_{-5.0}$	$1.18^{+0.34}_{-0.28}$

Notes: A summary of the weak-lensing mass measurements (M_{weak}) and X-ray determined masses within the same radii ($M_{\text{X,weak}}$). Column 2 lists the radii (r_{weak}) within which the weak-lensing mass measurements were made. Errors on the $M_{\text{X,weak}}$ values are 90 per cent confidence limits. Errors on the mass ratios mark the maximum and minimum values consistent with the joint confidence limits on the M_{weak} and $M_{\text{X,weak}}$ values. References for the weak-lensing data are as follows: RXJ1347.5-1145 from Fischer & Tyson (1997). Abell 2390 from Squires et al. (1997b). Abell 2744 (AC118) from Smail et al. (1997). Abell 2163 from Squires et al. (1997a). Abell 2218(a) from Squires et al. (1996) and (b) from Smail et al. (1997). AC114 from Natarajan et al. (1997).

uncertainty), in good agreement with the X-ray determined value, $M_{\text{X,weak}} = 7.6^{+0.8}_{-0.7} \times 10^{14}$ $M_\odot$, reported here. In addition, from their study of the cooling-flow cluster Abell 2390, Squires et al. (1997b) measure (from their fig. 3) a mass within $r = 200$ arcsec (940 kpc) of $10 \pm 4 \times 10^{14}$ $M_\odot$, in excellent agreement with the X-ray determined value of $8.2^{+8.7}_{-3.0} \times 10^{14}$ $M_\odot$.

From their weak-lensing analysis of *HST* images, Smail et al. (1997) measure a mass within the central 400 kpc (radius) region of Abell 2744 (AC118) of $3.70 \pm 0.64 \times 10^{14}$ $M_\odot$. This compares to the value determined from the X-ray analysis presented here of $2.33^{+0.31}_{-0.24} \times 10^{14}$ $M_\odot$ (implying a weak-lensing/X-ray mass ratio of $1.59^{+0.49}_{-0.43}$).

From their analysis of weak lensing in the most X-ray luminous cluster of galaxies known, RXJ1347.5-1145, Fischer & Tyson (1997) determine a mass within 2 Mpc of $3.4 \pm 0.8 \times 10^{15}$ $M_\odot$. This is in excellent agreement with the value of $3.6^{+1.1}_{-1.7} \times 10^{15}$ $M_\odot$ determined from the multiphase X-ray analysis presented here.

The weak-lensing masses for the clusters in our sample, and the X-ray-determined masses within the same regions, are summarized in Table 7. These results are shown in graphical form in Fig. 3 (together with the strong-lensing and X-ray results for the cooling-flow clusters using the more detailed lensing models; Section 4.3). The weak-lensing and X-ray mass values generally exhibit good agreement, for both cooling-flow and non-cooling-flow systems. We note again, however, that such agreement would not have been obtained for the cooling-flow clusters if the effects of the cooling flows on the X-ray data had not been accounted for (Section 4.2). We conclude that the enhancements of the lensing masses with respect to the X-ray-determined values for the non-cooling-flow clusters, inferred from the strong-lensing analyses, are limited to small ($r \lesssim 150$ kpc) radii. In the following section, we shall explore how even these discrepancies may be resolved.

4.6 Cluster core radii and cooling flows

The results on the cluster core radii determined from the X-ray analyses (Table 4, column 6) demonstrate a clear segregation between the cooling-flow and non-cooling-flow systems. The

mean core radius determined for the six cooling-flow clusters is ~50 kpc (with a trend for slightly larger core radii in the more X-ray luminous systems). For the two intermediate systems the value is 80 kpc, and for the five clear non-cooling flows the value is ~300 kpc. For the cooling-flow clusters for which lensing studies provide an independent measure of the mass core radius (PKS0745-191, MS2137.3-2353 and Abell 2390), excellent agreement between the X-ray and lensing results is observed. This result on the core radii, together with the agreement of the X-ray and lensing masses for the cooling-flow clusters (Sections 4.1–4.3, 4.5) and the alignment of the X-ray and lensing centroids (Section 4.4), strongly suggests that the assumptions of hydrostatic equilibrium and approximate isothermality in the mass-weighted temperature profiles in the cluster cores (Section 3.2) are valid. For cooling-flow clusters, both the X-ray and gravitational lensing measurements appear to provide an accurate description of the gravitating matter.

The results on the offsets of the X-ray and lensing centres for the non-cooling-flow clusters (Section 4.4) showed that in the central regions of these clusters, the X-ray gas is not in hydrostatic equilibrium with the gravitational potentials inferred from the strong-lensing data. The mass distributions in the non-cooling-flow clusters generally appear complex, consisting of two or more large mass clumps (Section 4.3), and must be evolving rapidly. If the assumptions of hydrostatic equilibrium and spherical symmetry used in the X-ray analyses are not valid, and the central ICM in these clusters has been shocked and disturbed by recent (or ongoing) merger events, then the core radii inferred from the X-ray data may overestimate the core radii of the total gravitating matter distributions in the dominant mass clumps. Such a suggestion is consistent with the results from numerical simulations (Roettiger et al. 1996) and is in agreement with the results for Abell 2219, presented here, for which the X-ray data suggest a core radius of ~200 kpc, whereas the detailed lensing analysis of Smail et al. (1995a) determines a core radius for the dominant mass clump of 46 ± 20 kpc, in good agreement with the values inferred for the relaxed cooling-flow clusters.

Table 8. The X-ray masses for the non-cooling-flow clusters for a fixed 50 kpc mass core radius.

	r_{arc} (kpc)	M_{arc} (10^{13} $M_\odot$)	M_{X,r_c50} (10^{13} $M_\odot$)	RATIO ($M_{arc}/M_{X,r_c50}$)
NON COOLING FLOWS				
Abell 2744(2)	119.6	11.36 (9.23)	$8.71^{+1.35}_{-0.76}$	$1.30^{+0.13}_{-0.17}$ ($1.06^{+0.10}_{-0.14}$)
Abell 2163	67.7	4.29	$6.09^{+0.60}_{-0.57}$	$0.70^{+0.08}_{-0.06}$
Abell 2218(#359)	79.4	5.42	$4.61^{+0.34}_{-0.44}$	$1.18^{+0.12}_{-0.09}$
Abell 2218(#384)	84.8	4.96	$4.96^{+0.37}_{-0.47}$	$1.00^{+0.10}_{-0.07}$
Abell 2219 (100 kpc)	100	11 ± 2	$7.76^{+0.84}_{-1.10}$	$1.42^{+0.53}_{-0.37}$
AC114 (75 kpc)	75.0	4.2 ± 0.1	$5.18^{+0.95}_{-0.77}$	$0.81^{+0.19}_{-0.14}$
INTERMEDIATE				
Abell 963	79.8	5.85	$3.78^{+0.52}_{-0.39}$	$1.55^{+0.18}_{-0.19}$
Abell 1689	183	30.7 (27.5)	$14.7^{+1.8}_{-1.5}$	$2.09^{+0.24}_{-0.23}$ ($1.87^{+0.21}_{-0.20}$)

Notes: The modified X-ray mass results for the non-cooling-flow and intermediate clusters with the assumption of hydrostatic equilibrium relaxed, and a fixed core radius for the mass distributions of 50 kpc adopted. M_{arc} and r_{arc} are the strong-lensing masses and radii within which those masses are evaluated. Where possible, we have used the results from the more sophisticated lensing analyses discussed in Section 4.3. M_{X,r_c50} values are the X-ray masses within the same radii (and their formal 90 per cent errors) determined with the fixed 50 kpc core radius. By relaxing the hydrostatic assumption and adopting core radii for the mass distributions in agreement with the mean value determined for the relaxed cooling-flow clusters, we can account for the bulk of the discrepancies between the strong-lensing and X-ray masses.
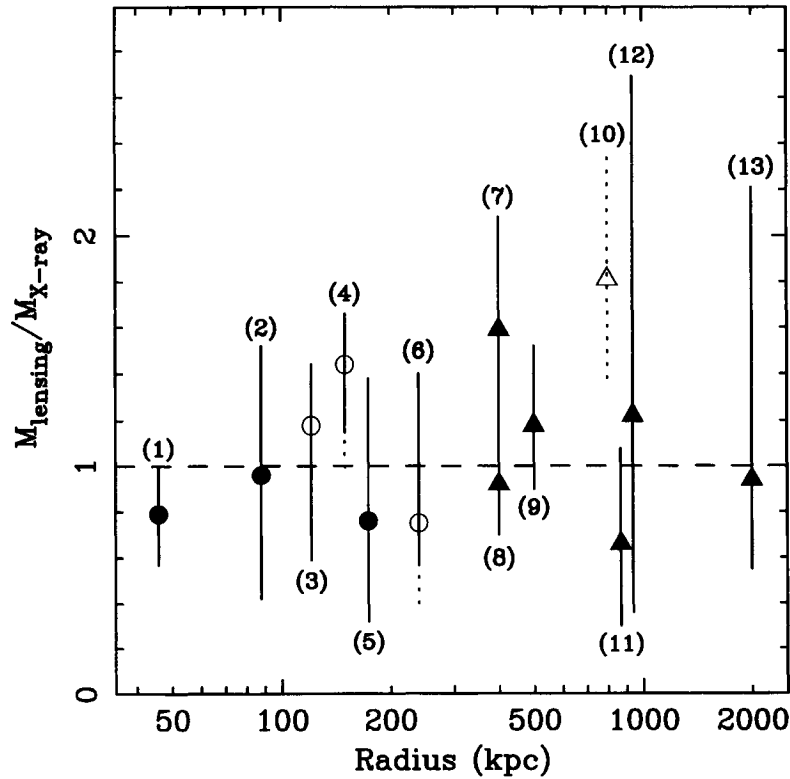

Figure 3. The ratio of lensing (strong and weak) and X-ray masses for those clusters for which a reliable and direct comparison of these values can be made. The ratios of the strong-lensing and X-ray masses are plotted as circles. Strong lensing results are only presented for the cooling-flow clusters since, for the non-cooling-flow and intermediate systems, the hydrostatic assumption is not expected to hold (Sections 4.4, 4.6). Filled circles show the results obtained with the detailed lensing models (Section 4.3) and open circles the results from the simple, spherically symmetric lensing models (which are only used when results from more detailed modelling are not available). The weak-lensing results (Section 4.5) are plotted as triangles. The open triangle is the Squires et al. (1996) result for Abell 2218 at a radius 800 kpc. The figure demonstrates excellent agreement between the gravitational lensing and X-ray masses for all clusters in our sample, for which reliable comparisons of these values can be made. The numbers in parentheses are used to identify the clusters; (1) PKS0745–191, (2) MS2137.3–2353, (3) MS1358.4+6245, (4) Abell 1835, (5) Abell 2390, (6) RXJ1347.5–1145, (7) Abell 2744, (8) Abell 2218 at 400 kpc, (9) AC114, (10) Abell 2218 at 800 kpc, (11) Abell 2163, (12) Abell 2390, (13) RXJ1347.5–1145.

We have examined whether inflation of the X-ray core radii, as a result of rapid evolution in the cluster potentials, can provide an explanation for the strong-lensing/X-ray mass discrepancies in the non-cooling-flow clusters. To do this, we have estimated the masses within the arc radii that are implied when adopting a fixed core radius of 50 kpc (in agreement with the mean core radius determined for the cooling-flow systems). The temperatures measured from the *ASCA* spectra, which define the velocity dispersions used to parametrize the mass distributions (Table 4), were assumed to maintain a reasonable representation of the virial temperatures of the clusters. (The simulations discussed in Section 4.1 suggest this to be reasonable.) Note that under the standard assumption of hydrostatic equilibrium in the X-ray gas, the use of such small core radii in the deprojection analyses would imply sharply rising temperature profiles in the central regions of the non-cooling-flow clusters, which are not, in general, observed in similar nearby systems, e.g. Markevitch & Vikhlinin (1997), Ohashi et al. (1997). See also the discussions by Miralda-Escudé & Babul (1995) and Waxman & Miralda-Escudé (1995).

The masses within the arc radii for the non-cooling flow clusters, calculated using a fixed core radius of 50 kpc and the velocity dispersions listed in Table 4, are summarized in Table 8. Also listed are the masses within the same radii inferred from the strong-lensing data. Where possible, the results from the more detailed lensing models discussed in Section 4.3 have been used. We see that the effects of over-estimating the gravitational core radii, from the X-ray data, can fully account for the discrepancies between the strong-lensing and X-ray masses for the non-cooling-flow clusters. Only for the intermediate cluster, Abell 1689, do such affects significantly fail to account for the differences between the mass measurements. For Abell 1689, it appears that material external to the X-ray luminous parts of the cluster, viewed in projection along the line of sight to the cluster core, is contributing to the lensing mass (Teague, Carter & Gray 1990; Girardi et al. 1997). If this material is not virialized and/or the gas density in it is low, then it will not significantly affect the X-ray emission observed.

4.7 Cooling flows and the probability of detecting strong lensing

Bartelmann & Steinmetz (1996) discussed how most detections of strong lensing in clusters are expected to be made in clusters of intermediate rather than exceptionally high X-ray luminosity, and how such detections will be biased (in samples of clusters selected on the basis of their strong lensing properties) towards systems that are dynamically active (i.e. systems in the process of virialization or undergoing merger events). A significant fraction (6/14) of the clusters in our sample have strong cooling flows and exhibit little or no obvious substructure at optical or X-ray wavelengths. However, these clusters are also amongst the most X-ray luminous and, by implication, most massive systems known. At such high X-ray luminosities, even a regular, relaxed cluster presents a significant surface area above the critical surface density for strong lensing. At lower X-ray luminosities (and masses), however, the area above the critical density is reduced, until for $L_X < 10^{45}$ erg s^{-1}, the probability of detecting strong lensing in a relaxed cluster becomes small. This point is illustrated in Fig. 4, where we plot the critical lensing radius (the putative arc radius) for three simulated cooling-flow clusters. The clusters have velocity dispersions (using the parametrization detailed in Section 3.2) of 1000, 700 and 600 km s^{-1}, corresponding to X-ray luminosities of $\sim 4 \times 10^{45}$, $\sim 1 \times 10^{45}$, and a few $\times 10^{44}$ erg s^{-1}, respectively. A fixed core
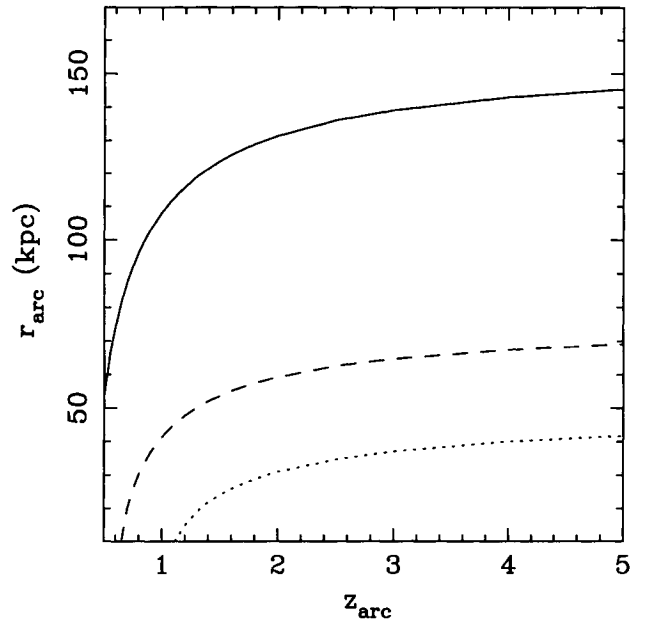

Figure 4. The critical radius for strong lensing (putative arc radius) as a function of the redshift of potential gravitational arcs in three simulated cooling-flow clusters (Section 4.7). The solid curve is for a cluster with $\sigma = 1000$ km s^{-1} (corresponding to $L_X \sim 4 \times 10^{45}$ erg s^{-1}; cf. Abell 1835). The dashed curve is for $\sigma = 700$ km s^{-1} ($L_X \sim 10^{45}$ erg s^{-1}) and the dotted curve for $\sigma = 600$ km s^{-1} ($L_X \sim$ a few $\times 10^{44}$ erg s^{-1}). A fixed core radius of 50 kpc and a cluster redshift, $z = 0.3$, are assumed.

radius of 50 kpc, a cluster redshift of $z = 0.3$, and spherical symmetry are assumed. We see that for a luminous ($\sigma = 1000$ km s^{-1}) cooling-flow cluster at $z = 0.3$, the critical radius varies from $50 - 150$ kpc for arc redshifts, $z_{arc} = 0.5 - 5.0$. At luminosities of only a few $\times 10^{44}$ erg s^{-1}, however, the critical radius is $\lesssim 40$ kpc, and the probability of detecting strong lensing is therefore low. At such low/intermediate X-ray luminosities, then, the bulk of the detections of strong lensing will occur in dynamically active clusters where projection effects enhance the lensing signal. In samples of lensing clusters with low to intermediate X-ray luminosities ($L_{X,2-10} < 10^{45}$ erg s^{-1}), few clusters with large cooling flows (in relation to the total cluster luminosity) are expected to be found.

Finally, we note that a number of other well-known strong-lensing clusters have recently undergone, or are awaiting, detailed *ASCA* and *ROSAT* HRI X-ray observations, e.g. Cl0024+17, Cl0302+17, Abell 2104 and Cl2244-02. Comparisons with the results obtained for those systems, using analysis techniques similar to those discussed here, will provide an interesting test of the conclusions we have drawn.

5 CONCLUSIONS

The main conclusions from this work may be summarized as follows.

(i) Determinations of cluster masses from X-ray and strong gravitational lensing data show excellent agreement for cooling-flow clusters (which are typically dynamically relaxed systems). This implies that thermal pressure dominates over non-thermal processes in the support of the X-ray gas against gravity in these systems, and that the hydrostatic assumption used in the X-ray mass determinations is valid.

(ii) The mean core radius for the gravitating matter in the cooling-flow clusters, determined from the X-ray data, is ∼50 kpc (where the core radii have been defined using an isothermal parametrization for the total mass profiles). Comparisons to measurements of the core radii from detailed gravitational-lensing studies show excellent agreement, lending further support to the conclusions given in (i).

(iii) For the non-cooling-flow clusters, the masses determined from the strong-lensing data exceed the X-ray values by a factor of 2−4. However, significant offsets between the X-ray and lensing centres are observed, indicating that the X-ray and strong-lensing data are probing different lines of sight through the clusters. These offsets, and the generally complex dynamical states of the clusters inferred from their X-ray morphologies, lensing data and galaxy distributions, suggest that the gravitational potentials in the central regions of the non-cooling flow systems are evolving rapidly, and that the assumption of hydrostatic equilibrium involved in the X-ray mass measurements is likely to have broken down. The discrepancies between the X-ray and strong-lensing mass measurements may be reconciled if the dynamical activity has caused the X-ray analyses to overestimate the core radii of the dominant mass clumps in the clusters. Substructure and line-of-sight alignments of material towards the cluster cores may also contribute to the discrepancies, since they will increase the probability of detecting gravitational arcs in the clusters and can enhance the lensing masses without significantly affecting the X-ray data.

(iv) Comparisons of the X-ray mass measurements on larger scales with measurements from weak gravitational lensing studies show excellent agreement for both the cooling-flow and non-cooling-flow systems.

(v) We have highlighted the importance of accounting for cooling flows in X-ray determinations of cluster masses. The inappropriate use of simple isothermal spectral models in the analysis of X-ray data for clusters with massive cooling flows will result in significant underestimates of their virial (X-ray) temperatures and masses.

ACKNOWLEDGMENTS

REFERENCES

Allen S. W., Fabian A. C., 1994, MNRAS, 269, 409
Allen S. W., Fabian A. C., 1997, MNRAS, 286, 583
Allen S. W., Fabian A. C., Edge A. C., Böhringer H., White D. A., 1995, MNRAS, 275, 741
Allen S. W., Fabian A. C., Kneib J.-P., 1996a, MNRAS, 279, 615
Allen S. W., Fabian A. C., Edge A. C., Bautz M. W., Furuzawa A., Tawara Y., 1996b, MNRAS, 283, 263
Arnaud K. A., 1996, in Jacoby G., Barnes J., eds, Astronomical Data Analysis Software and Systems V. ASP Conf. Ser. 101, Astron. Soc. Pac., San Francisco, p. 17
Balucinska-Church M., McCammon D., 1992, ApJ, 400, 699
Bartelmann M., 1995, A&A, 299, 11
Bartelmann M., Steinmetz M., 1996, MNRAS, 283, 431
Binney J., Tremaine S., 1987, Galactic Dynamics. Princeton Univ. Press, Princeton NJ
Buote D. A., Tsai J. C., 1996a, ApJ, 457, 565
Buote D. A., Tsai J. C., 1996b, ApJ, 458, 27
Couch W. J., Sharples R. M., 1987, MNRAS, 229, 423
David L. P., Jones C., Forman W., 1995, ApJ, 445, 578
David L. P., Harnden F. R., Kearns K. E., Zombeck M. V., 1996, The *ROSAT* HRI Calibration Report. ftp://legacy.gsfc.nasa.gov/rosat/doc/hri/hri_report
Dickey J. M., Lockman F. J., 1990, ARA&A, 28, 215
Ebbels T. M. D., Le Borgne J.-F., Pelló R., Ellis R. S., Kneib J.-P., Smail I., Sanahuja B., 1996, MNRAS, 281, L75
Ebeling H., Voges W., Böhringer H., Edge A. C., Huchra J. P., Briel U. G., 1996, MNRAS, 281, 799
Ebeling H., Edge A. C., Böhringer H., Allen S. W., Crawford C. S., Fabian A. C., Voges W., Huchra J. P., 1998, MNRAS, submitted
Edge A. C., Stewart G. C., Fabian A. C., 1992, MNRAS, 255, 431
Eke V. R., Cole S., Frenk C. S., 1996, MNRAS, 282, 263
Ellis R. S., Allington-Smith J., Smail I., 1991, MNRAS, 249, 184
Evrard A., 1990, ApJ, 363, 349
Evrard A., Metzler C. A., Navarro J. F., 1996, ApJ, 469, 494
Fabian A. C, 1994, A&AR, 32, 277
Fabian A. C., Hu E. M., Cowie L. L., Grindlay J., 1981, ApJ, 248, 47
Fischer P., Tyson J. A., 1997, AJ, 114, 14
Fort B., Mellier Y., 1994, A&AR, 5, 239
Fort B., Le Fèvre O., Hammer F., Cailloux M., 1992, ApJ, 399, L125
Franx M., Illingworth G. D., Kelson D. D., van Dokkum P. G., Tran K., 1997, ApJ, 486, L75
Frenk C. S., White S. D. M., Efstathiou G., Davis M., 1990, ApJ, 351, 10
Fukazawa Y., Ohashi T., Fabian A. C., Canizares C. R., Ikebe Y., Makashima K., Mushotzky R. F., Yamashita K., 1994, PASJ, 46, L55
Gioia I. M., Maccacaro T., Schild R. E., Wolter A., Stocke J. T., Morris S. L., Henry J. P., 1990, ApJS, 72, 567
Girardi M., Fadda D., Escalera E., Giuricin G., Mardirossian F., Mezzetti M., 1997, ApJ, 490, 56
Gudehus D. H., 1989, ApJ, 340, 661
Henry J. P., Arnaud K. A., 1991, ApJ, 372, 410
Johnstone R. M., Fabian A. C., Edge A. C., Thomas P. A., 1992, MNRAS, 255, 431
Jones C., Forman W., 1984, ApJ, 276, 38
Kaastra J. S., Mewe R., 1993, Legacy, 3, HEASARC, NASA
Kitayama T., Suto Y., 1996, ApJ, 469, 480
Kneib J.-P., Mellier Y., Fort B., Mathez G., 1993, A&A, 273, 367
Kneib J.-P., Mellier Y., Pelló R., Miralda-Escudé J., Le Borgne J.-F., Böhringer H., Picat J.-P., 1995, A&A, 303, 27
Lavery R. J., Henry J. P., 1988, ApJ, 329, 21L
Le Borgne J. F., Pelló R., Sanahuja B., 1992, A&AS, 95, 87
Loeb A., Mao S., 1994, ApJ, 435, 109L
Lucey J. R., 1983, MNRAS, 204, 33
Markevitch M., 1997, ApJ, 491, 467
Markevitch M., Vikhlinin A., 1997, ApJ, 474, 84
McGlynn T. A., Fabian A. C., 1984, MNRAS, 208, 709
Mellier Y., Fort B., Kneib J.-P., 1993, ApJ, 407, 33
Miralda-Escudé J., Babul A., 1995, ApJ, 449, 18
Natarajan P., Kneib J.-P., Smail I., Ellis R. S., 1997, preprint, astro-ph/9706129
Navarro J. F., Frenk C. S., White S. D. M., 1995, MNRAS, 275, 720
Nulsen P. E. J., Böhringer H., 1995, MNRAS, 274, 1093
Ohashi T., Honda H., Ezawa H., Kikuchi K., 1997, in Makino F., Mitsuda K., eds, X-ray Imaging and Spectroscopy of Cosmic Hot Plasmas. Universal Academy Press, Tokyo, p. 49
Oukbir J., Blanchard A., 1997, A&A, 317, 10
Oukbir J., Bartlett J. G., Blanchard A., 1997, A&A, 320, 365
Pelló R., Sanahuja B., Le Borgne J. F., Soucail G., Mellier Y., 1991, ApJ, 366, 405
Pelló R., Le Borgne J. F., Sanahuja B., Mathez G., Fort B., 1992, A&A, 266, 6

Peres C. B., Fabian A. C., Edge A. C., Allen S. W., Johnstone R. M., White D. A., 1997, MNRAS, in press

Pierre M., Le Borgne J. F., Soucail G., Kneib J.-P., 1996, A&A, 311, 413

Porter A. C., Schneider D. P., Hoessel J. G., 1991, AJ, 101, 1561

Roettiger K., Burns J. O., Loken C., 1996, ApJ, 473, 651

Schindler S., 1996, A&A, 305, 756

Schindler S., Hattori M., Neumann D. M., Böhringer H., 1997, A&A, 317, 646

Smail I., Ellis R. S., Fitchett M. L., Norgaard-Nielsen H. U., Hansen L., Jorgensen H. E., 1991, MNRAS, 252, 19

Smail I., Hogg D. W., Blandford R., Cohen J. G., Edge A. C., Djorgovski S.G., 1995a, MNRAS, 277, 1

Smail I., Couch W. J., Ellis R. S., Sharples R. M., 1995b, ApJ, 440, 501

Smail I., Ellis R. E., Dressler A., Couch W. J., Oemler A., Sharples R. M., Butcher H., 1997, ApJ, 479, 70

Soker N., Sarazin C. L., 1990, ApJ, 348, 73

Squires G., Kaiser N., Babul A., Fahlman G., Woods D., Neumann D. M., Böhringer H., 1996, ApJ, 461, 572

Squires G., Neumann D. M., Kaiser N., Arnaud M., Babul A., Böhringer H., Fahlman G., Woods D., 1997a, ApJ, 482, 648

Squires G., Kaiser N., Fahlman G., Babul A., Woods D., 1997b, ApJ, 469, 73

Sutherland W., 1988, MNRAS, 234, 159

Tanaka Y., Inoue H., Holt S.S., 1994, PASJ, 46, L37

Teague P. F., Carter D., Gray P.M., 1990, ApJS, 72, 715

Thomas P. A., Fabian A. C., Nulsen P. E. J, 1987, MNRAS, 228, 973

van Haarlem M. P., Frenk C. S., White S. D. M., 1997, MNRAS, 287, 817

Viana P. T. P., Liddle A. R., 1996, MNRAS, 281, 323

Waxman E., Miralda-Escudé J., 1995, ApJ, 451, 451

White D. A., Fabian A. C., 1995, MNRAS, 273, 72

White D. A., Jones C., Forman W., 1997, MNRAS, 292, 419

White S. D. M., Efstathiou G., Frenk C. S., 1993, MNRAS, 262, 1023

Wu X., Fang L., 1997, ApJ, 483, 62

This paper has been typeset from a T_EX/L^AT_EX file prepared by the author.